Near–Monolayer Platinum Shell on Core–Shell Nanocatalysts for High–Performance Direct Methanol Fuel Cell

10 AUTHORS, INCLUDING:

Yaw-Wen Yang
National Synchrotron Radiation Research Cen…
120 PUBLICATIONS   1,160 CITATIONS
SEE PROFILE

Chih-Hao Lee
National Tsing Hua University
292 PUBLICATIONS   4,358 CITATIONS
SEE PROFILE

Ten-Chin Wen
National Cheng Kung University
275 PUBLICATIONS   5,454 CITATIONS
SEE PROFILE

Tsan-Yao Chen
National Tsing Hua University
53 PUBLICATIONS   353 CITATIONS
SEE PROFILE

Near-Monolayer Platinum Shell on Core−Shell Nanocatalysts for High-Performance Direct Methanol Fuel Cell

Jang-Jung Wang,[†,#] Yu-Ting Liu,[§,#] I-Li Chen,[‡] Yaw-Wen Yang,[∥] Tsung-Kuang Yeh,[†] Chih Hao Lee,[†,∥] Chi-Chang Hu,[‡] Ten-Chin Wen,[⊥] Tsan-Yao Chen,*[,†] and Tsang-Lang Lin*[,†]

[†]Department of Engineering and System Science and [‡]Department of Chemical Engineering, National Tsing Hua University, No. 101, Section 2, Kuang-Fu Road, Hsinchu 30013, Taiwan

[§]Department of Environmental Science and Engineering, Tunghai University, No. 181, Section 3, Taichung Port Road, Taichung 40704, Taiwan

[∥]National Synchrotron Radiation Research Center, 101 Hsin-Ann Road, Hsinchu 30076, Taiwan

[⊥]Department of Chemical Engineering, National Cheng Kung University, 1 University Road, Tainan 70101, Taiwan

S *Supporting Information*

ABSTRACT: We investigate the Ru_{core}-Pt_{shell} nanoparticles (NPs) with near-monolayer thick shell atoms as the electrocatalysts at anode in the direct methanol fuel cell (DMFC). The results of X-ray diffraction indicate that its crystal structure experienced a compressive strain in Pt shell region. The shell thickness of Ru_{core}-Pt_{shell} NPs was determined to be 1.5 atomic layers by small-angle X-ray scattering by using a core−shell scattering model, and the surface atomic morphology was illustrated via high-resolution transmission electron microscopy (HRTEM). Compared with the Pt NPs, the power density of DMFC with Ru_{core}-Pt_{shell} NPs was improved by ∼450% (from 17.1 to 92.8 mW cm^{-2} mg^{-1}), and the open-circuit voltage was improved by 0.18 V (from 0.49 to 0.67 V). Our results fulfill the development of cost-effective DMFC with outstanding performance.
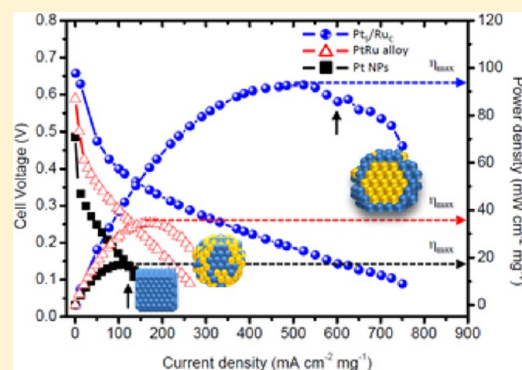
INTRODUCTION

The conformation and composition of electrocatalyst at anode are key factors determining the performances of direct-methanol fuel cells (DMFCs). Therefore, using minimal amount of noble metal for synthesizing electrocatalyst with outstanding methanol electrooxidation activity is considered to be the critical step in developing high-performance and cost-effective DMFC systems.[1,2] This crucial criterion can be achieved by manipulating the atomic structure at Pt-based electrocatalyst surface. One successful strategy is controlling the heteroatomic structure in electrocatalyst and improving the interconnection at the support. The heteroatomic structures in the Pt-based electrocatalyst generally include the homogeneous alloy catalysts, cluster-in-cluster, core−shell architecture, and so on.[3,4] Meanwhile the lattice strain in the platinum crystal lattice at the electrocatalyst-to-support interconnection has been found dominating the efficiency of cell operation[1,5] because all catalysts in DMFCs are deposited on the porous supports. Among all of the above heteroatomic structures, the core−shell architecture is a simple approach to manipulate the lattice strain and composition at the particle surface. By carefully selecting the core crystallite and precisely controlling the shell thickness while maintaining high specific surface area (m^2/g) via nanoparticle (NP) size, an outstanding electrochemical durability (potential cycles >10^5) in room temperature CO oxidation has been achieved.[1,6−11]

Moreover, from the studies on the heterogeneous catalysis by the density functional theory (DFT) simulations, the activity of core−shell electrocatalyst is mainly determined by the topmost monolayers of Pt atoms (∼4 to 5 Å depth) in the shell crystal.[1,11,12] However, because of the low electrochemical sustainability and reactivity, it is difficult to develop a cost-effective DMFC via the conventional catalyst technologies.

Our previous studies demonstrated that the surface activity and structure durability of core−shell electrocatalyst can be substantially improved by growing monolayer of electrochemically active atom (Pt) onto the small lattice parameter core crystal (Ru).[6,8−10,13] In this work, we further demonstrate the capability of Ru_{core}-Pt_{shell} NPs (Pt_S/Ru_C NPs) for improving the power efficiency of a full DMFC system. In comparing with PtRu alloy NPs and monometallic Pt NPs, the Pt_S/Ru_C NPs with a near-monolayer thick of Pt shell improve the power efficiency and current density of DMFC by >450%. To clarify the role of Pt_S/Ru_C in anode, details of the surface electronic properties of NPs correlating to the electrochemical performance of DMFC will be given in the latter sections. We will clarify which mechanism (e.g., bifunctional effect, ligand effect, lattice strain,
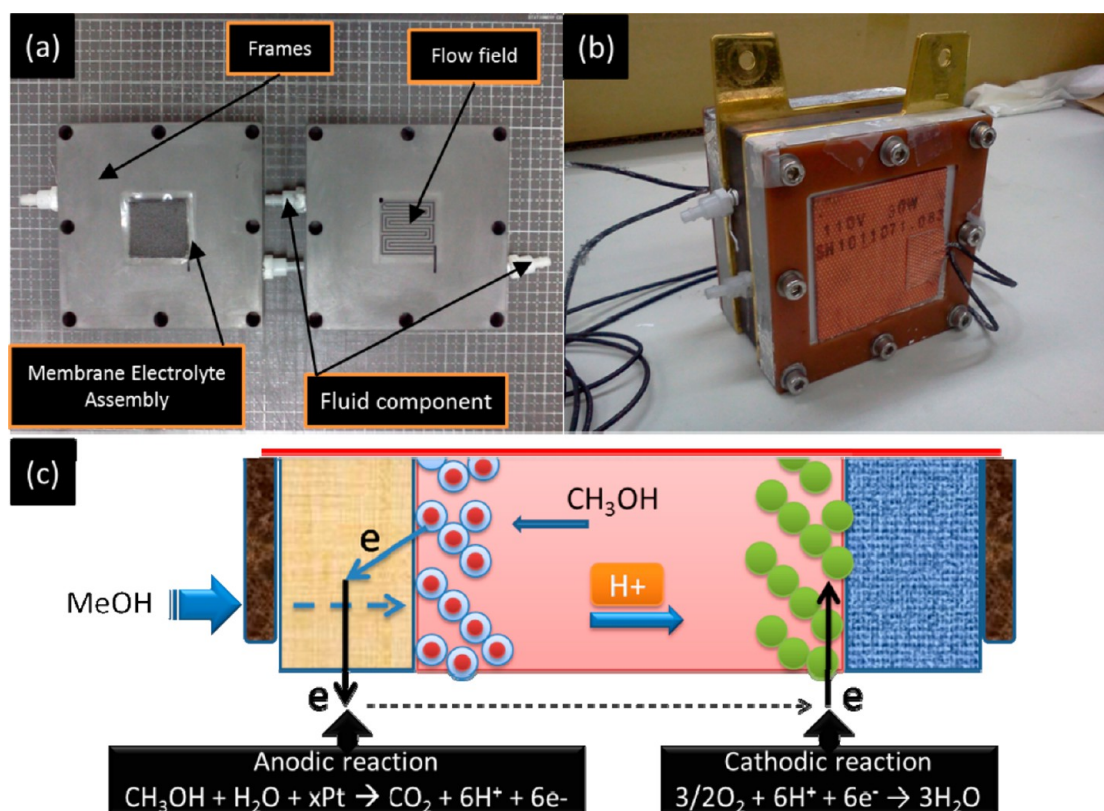
Figure 1. Scheme for assembly of DMFC full stack. (a) Devices of flow field, fluid components, frames, and membrane electrolyte assembly (MEA). (b) Assembled full stack. (c) Details of MEA component.

and surface atomic packing)[1,5,11,14] is the dominant factor in the catalytic performance of Pt_S/Ru_C NPs, and will show how the surface activities of bimetallic systems can be optimized through the control of the atomic structure of the nanocatalysts. To hit our target, the DMFCs with Pt NPs and PtRu alloy NPs are prepared, and the corresponding structure to electrochemical correlation is presented as a reference.

■ EXPERIMENTS

Synthesis of Pt NPs, PtRu Alloy NPs, and Ru$_{core}$–Pt$_{shell}$ NPs with Monolayer Shell Atoms. The Ru$_{core}$-Pt$_{shell}$ NPs were synthesized by a two-step polyol method with the adopted recipes and reaction sequences in conformity with the expected atomistic architecture. First, the hcp Ru cores with an average diameter of ~2.5 nm were prepared by reducing 100 mM ruthenium chlorite in ethylene glycol (EG) with the thermal treatments adopted from the previous work.[10] Second, the Pt shell of near monolayer atomic layer thick was produced basing on a heterogeneous nucleation and growth pathway by a thermal reduction of Pt anions ($H_2PtCl_6\cdot6H_2O$, 99 at%) on the surface of Ru cores in the presence of 10 wt % polyvinylpyrrolidone (PVP) stabilizer in EG.

Samples of polymer (PVP)-blended PtRu alloy NPs containing the Pt/Ru ratio of 1.0 (in a total metal content of ~0.6 to 0.7 wt %) were synthesized by simultaneously reducing the Pt and Ru precursors by using polyol method in a presence of PVP-40 stabilizer.[15] The mixture of reactants was stirred at 300 rpm for 30 min in a PYREX beaker (sealed on top with three open poles) prior to the heating processes. After mixing, the solution was heated to 160 °C by a temperature-programmable hot plate (Thermal, Super-Nuova Digital SP131825w with remote probe) with a stirring speed at 150 rpm and a nitrogen gas

purge (15 mL min⁻¹) for 2 h during the thermal reduction of NPs. The total concentration of metal precursors (Pt^{4+} + Ru^{3+} ions) was fixed in 10 mM, and the concentration of PVP-40 stabilizer was set to be 10 wt % with respective to whole system. For preparing the Pt NPs, the ruthenium content was set to be zero and the thermal conditions were identical to that of the processes for producing the PtRu alloy NPs.

Dispersion of NPs on the CNT/CF Substrate (NPs@ MWCNT/CF) and Assembly of DMFC Fuel-Cell Stack. The NPs@MWCNT/CF was used as the anode in DMFC system. The MEA system was assembled by three counterpart devices including a conventional cathode of Pt@carbon support (with a metal loading of ~1.0 mg cm⁻²), a NPs@CNT/CF (with a Pt loading of 0.32 to 1.31 mg cm⁻²) anode, and an electrolyte of proton exchange membrane (purchased from Sigma-Aldrich, Nafion-117), where the photos for components of a DMFC stack are shown in Figure 1. Multiwalled carbon nanotubes (MWCNTs) were directly synthesized on the iron deposited carbon cloth (MWCNTs/CF) by bias-assisted microwave plasma-enhanced chemical vapor deposition (PECVD) system. The details of synthesis processes of MWCNTs were described in our previous work.[16] For depositing the NPs onto the MWCNTs/CF substrate, the as-synthesized MWCNTs were modified by a dual-step modification process. They were initially treated with a 14 M HNO_3 solution for 2 h and subsequently transferred to a 14 M 2-mercaptoethanol (C_2H_6SO) solution for forming the surface thiolate group (in a dehydration reaction[16]) for supporting Pt NPs (see eq 1):
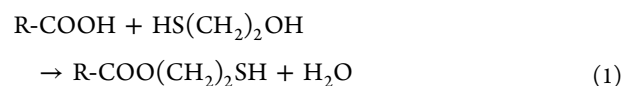
$$R\text{-}COOH + HS(CH_2)_2OH$$

$$\rightarrow R\text{-}COO(CH_2)_2SH + H_2O \qquad (1)$$

2254

dx.doi.org/10.1021/jp408012d | J. Phys. Chem. C 2014, 118, 2253−2262

Table 1. Measurement Parameters for the DMFC Fuel-Cell Stack

anode	NPs/functionalized MWCNTs/CF and Nafion (Pt = 0.32 to 1.31 mg cm^{-2})
cathode	Pt 1 mg cm^{-2} (Alfa) and Nafion 0.5 mg cm^{-2}
cathode feed	O$_2$ 100 sccm
anode feed	1 M MeOH 60 mL h^{-1}
operation temp.	70 °C
activation time	1 M H$_2$SO$_4$ 10 mL min^{-1} for 24 h
hot-press parameter	100 kgf cm^{-2} 120 °C for 180 s
screw pressure	20 kgf cm^{-2}
solid electrolyte	Du-Pont Nafion 117
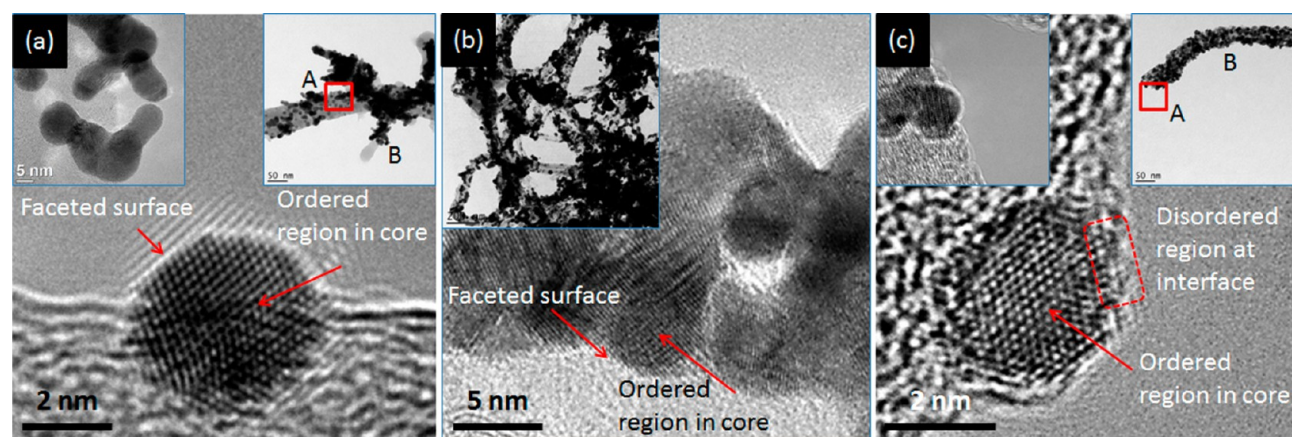
Figure 2. High-resolution transmission electron microscopy images of CNT-supported (a) Pt NPs, (b) PtRu alloy NPs, and (c) Pt$_S$/Ru$_C$ NPs.

This reaction was kept at 80 °C for 6 h. Finally, the residual C$_2$H$_6$OS was rinsed with highly purified ethanol solvent (Sigma-Aldrich, 99.95%). The dispersion of NPs on the modified substrate was conducted by the self-assembly method with the assistance of thiolate ligands at the MWCNT surface. After the thiolation treatment, the MWCNTs/CF electrode was immersed into the ethanol solution containing polymer blended NPs (~1 wt %) at room temperature for dispersing NPs and then dried for 30 min in air. Four immersion cycles were conducted to increase the metal loading in a compatible extent to that of commercial electrode (~1.0 mg cm^{-2}). For reinforcing the interconnection of NPs, the immersed MWCNTs/CF electrode was annealed at 330 °C for 30 min. The full-stack measurement conditions are listed in Table 1. Before assembling, a thin Nafion film was coated between interfaces of the device in improving the connectivity of proton exchange channels through the three counterparts (inside the MEA system). Details of the assembly processes are given in the Supporting Information.

NPs Characterizations. The microstructure of NPs was elucidated by high-resolution transmission electron microscopy (HRTEM). Physical properties of NPs were characterized by various X-ray spectroscopy techniques including small-angle X-ray scattering (SAXS), X-ray absorption spectroscopy (XAS), X-ray diffraction (XRD), and photoemission valence band (VB) spectroscopy at beamlines of BL-23A, BL-17C, BL-01C2, and BL-24A at NSRRC (Taiwan), respectively. The high-resolution XRD patterns were collected at beamline of BL-12B2 at Spring-8 (Japan). The methanol electrooxidation (MOR) activity of the NPs, which was correlated to their surface composition and structures, was determined by using CV analysis (CH Instruments model 600B). The electrochemical cell for CV analysis consisted of a working electrode, an Ag/AgCl reference electrode, and a 10 mm × 10 mm platinum foil counter electrode.[10,16]

Electrochemical Experiments on the DMFC Assembly and Measurements. The installation of DMFC stack can be conducted in six steps: (1) Preparing the MEA module by the above three steps mentioned in Supporting Information; (2) placing the spacing membrane in two sides of the MEA in preventing the shorting of electrochemical circuits and sealing the MEA; (3) placing the conducting graphite with flow pattern at outer side of spacing membrane; (4) mounting the copper plate at the flow pattern for collecting the electrochemical current; (5) mounting the heating plate at the current collector; and (6) fixing the DMFC stack with the scroll. The installed DMFC stack with connection cables and fuel channels is presented in the Supporting Information. After the DMFC stack was fixed, the MEA inside the stack was activated by flowing with 0.5 M of H$_2$SO$_4$ solution for 24 h and then connected with 850e cables and fuel suppliers prior to the electrochemical measurement. During the measurement, the stack was heated to 30, 50, and 70 °C and fed by 1.0 M of methanol solution with the flux of 60 mL/h at anode and the 100 sccm of oxygen flow at cathode at the identical temperature of the DMFC stack, respectively. The entire stack was stabilized for at least 30 min (or at a stable open circuit voltage) prior to the electrochemical (I–V curve and power density) measurement.

■ RESULTS AND DISCUSSION

Particle Shape and Crystal Structure of NPs. The HRTEM was employed to investigate not only the crystal structure but also the near surface atomic arrangements of the NPs. Figure 2a−c, respectively, demonstrates the HRTEM images of CNT-supported Pt NPs, PtRu alloy, and Pt$_S$/Ru$_C$ NPs after annealing at 330 °C for 30 min; the insets show the corresponding TEM images. From Figure 2a,b, the drop-like particle with indistinct interparticle boundaries indicates the sintering between the Pt NPs and PtRu alloy at CNT. It implies
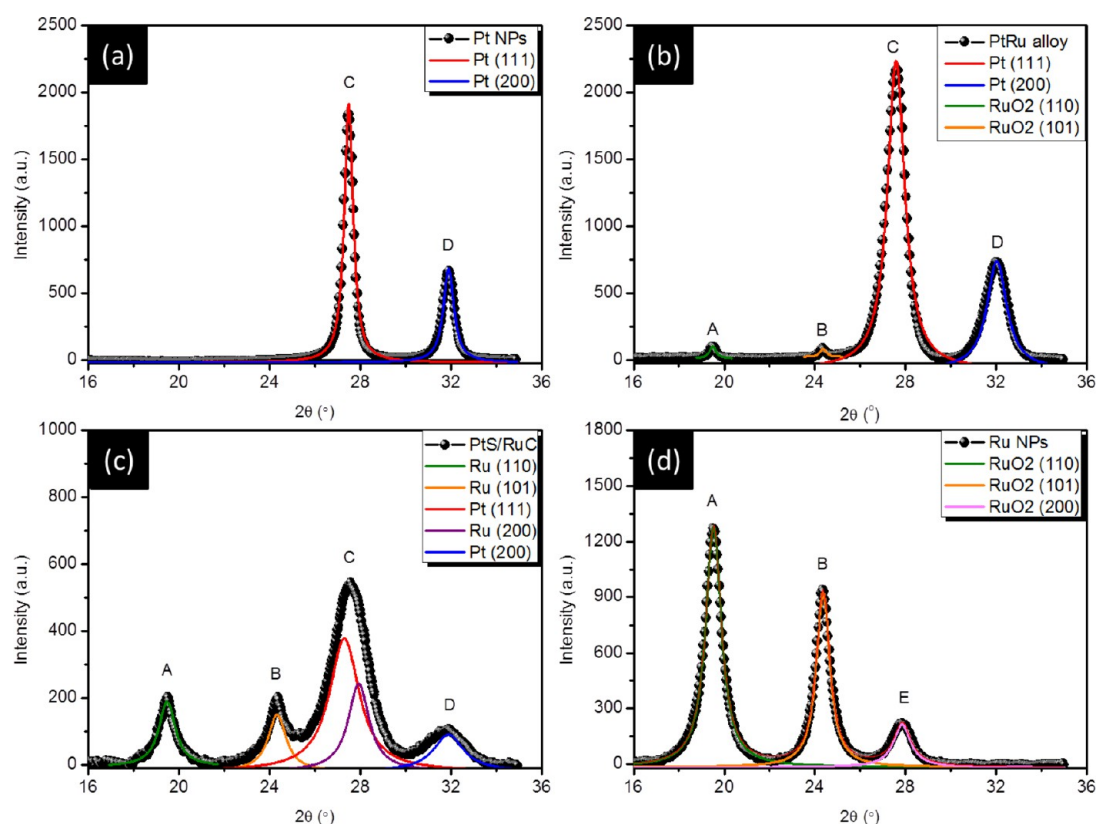
2255

dx.doi.org/10.1021/jp408012d | J. Phys. Chem. C 2014, 118, 2253−2262

Figure 3. XRD patterns with fitting curves of annealed Pt NPs (3a), PtRu alloy NPs (3b), Pt$_S$/Ru$_C$ NPs (3c), and Ru NPs (3d). The peaks A–E denote the diffraction lines of RuO$_2$ (110), RuO$_2$ (101), Pt (111)/Ru(200), Pt (200), and RuO$_2$(200), respectively. The diffraction patterns were collected by using an incident X-ray wavelength of 1.07229 Å (at 11 564 eV).

Table 2. Structure Parameters of Pt NPs, PtRu Alloy, and Pt$_S$/Ru$_C$ NPs with Thermal Annealing at 330 °C for 30 min[a]

NPs	peak	index	2θ	$\Delta 2\theta$	ζ (Å)[b]	d (Å)	ε (%)[c]
Pt NPs	C	Pt(111)[d]	27.491	0.46	64.2	2.266	
	D	Pt(200)[d]	31.897	0.56	53.4	1.959	
PtRu alloy	A	RuO$_2$(110)[e]	19.497	0.346	84.9	3.180	
	B	RuO$_2$(101)[e]	24.365	0.323	91.7	2.551	
	C	Pt(111)[d]	27.581	0.924	32.3	2.258	−0.32
	D	Pt(200)[d]	32.027	1.052	28.7	1.851	−0.54
Pt$_S$/Ru$_C$	A	RuO$_2$(110)[e]	19.490	0.88	33.5	3.181	
	B	RuO$_2$(101)[e]	24.335	0.97	30.5	2.554	
	C	Pt(111)[d]	27.300	1.59	18.7	2.282	0.82
	D	Pt(200)[d]	31.891	1.62	18.6	1.960	0.00
Ru NPs	A	RuO$_2$(110)[e]	19.523	0.85	34.7	3.176	
	B	RuO$_2$(101)[e]	24.362	0.73	40.8	2.552	
	E	RuO$_2$(200)[e]	27.854	0.94	31.6	2.237	

[a]Data were estimated from the XRD patterns. [b]ζ: coherent length. [c]ε: lattice strain. [d]ICSD # 041525 Pt f.c.c. phase. [e]ICSD # 084619 RuO$_2$ orthorhombic phase.

two fatal issues of Pt NPs for electrochemical applications, including the high surface free energy of crystalline facets and the lack of sublayer or local heteroatom neighbors. The former leads to the interparticle sintering, and the latter triggers the relocation of outmost Pt atoms. Both of the two crystal restructure pathways (induced by reducing the total surface free energy)[12] result in the increase in crystal size, thus decreasing the number of surface active sites on such catalyst. Given that the dispersion of catalysts on CNT was improved by the predispersion microwave-assisted surface thiolation treatment, the substantial interparticle sintering reveals the weak heterogeneous attachment at the CNT surface and the strong self-aggregation of Pt

NPs in solution,[17] therefore resulting in their poor thermal stability. Similar to the Pt NPs, the severe interparticle sintering of PtRu alloy NPs is unavoidable. (See Figure 2b.) Both the Pt NPs and PtRu alloy NPs at CNTs comprise the faceted surfaces, and the ordered core region indicates the formation of fcc phases, which are consistent with the XRD analysis. (See Figure 3.) The Pt$_S$/Ru$_C$ NPs are particles in the hexagonal shape containing a disordered interface region and an ordered core region (Figure 2c). It indicates the preferential growth of Pt shell crystal at the (111) plane, being regarded as a multifaceted core−shell architecture.[6,7,18] The lattice strain evolution along with the growth of Pt shell crystal is consistently predicted by the DFT
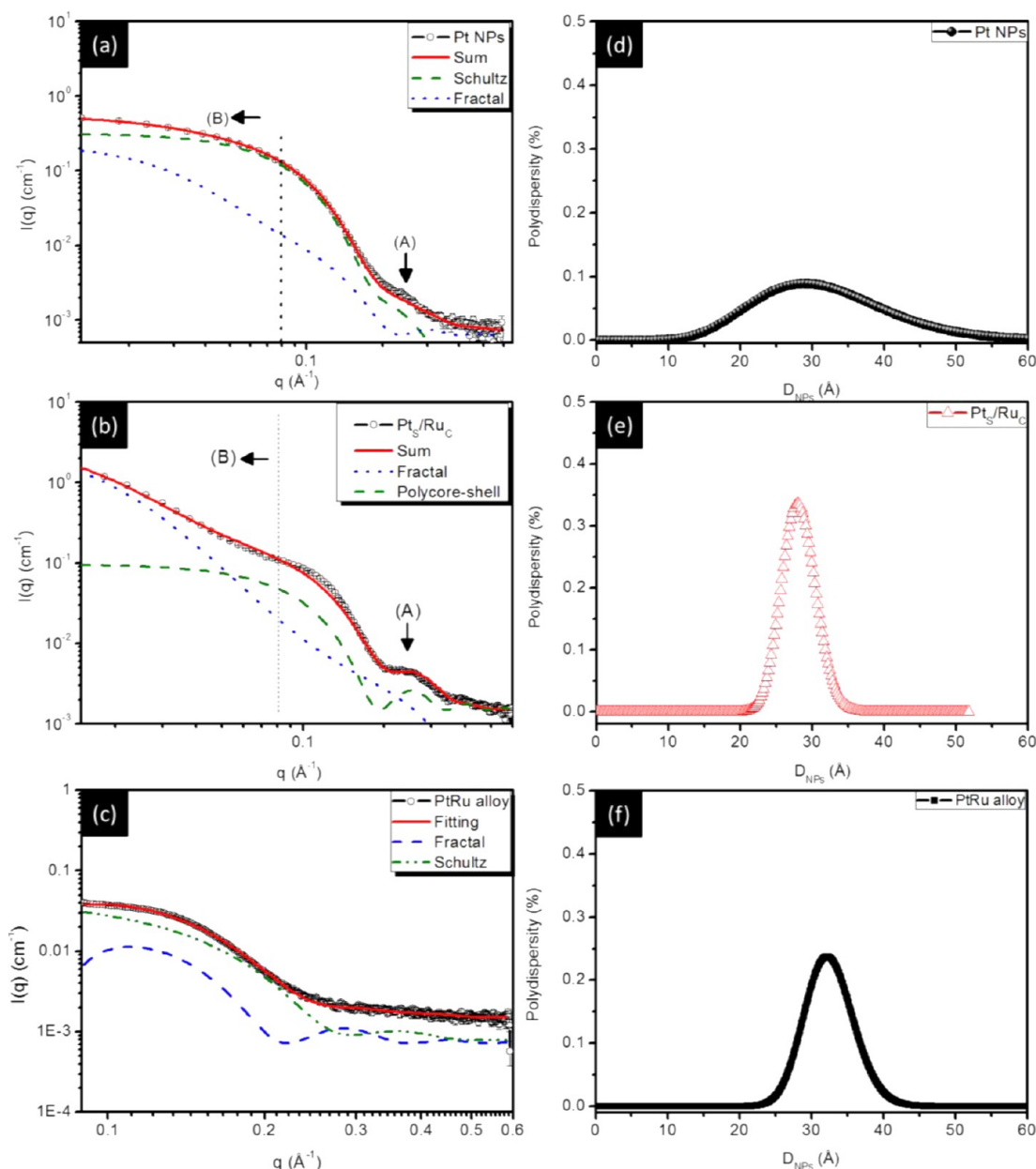
2256

dx.doi.org/10.1021/jp408012d | J. Phys. Chem. C 2014, 118, 2253–2262

Figure 4. Author: SAXS spectra of (a) Pt NPs, (b) Pt_S/Ru_C NPs, and (c) PtRu alloy and the particle size polydispersity of (d) Pt NPs, (e) Pt_S/Ru_C NPs, and (f) PtRu alloy (blue line: fitting curve of interparticle aggregate; green line: the fitting curves of Schultz sphere for Pt NPs and the core−shell structure with polydispersed core size model for Pt_S/Ru_C NPs, respectively; red line: sum of the two models).

calculation in literatures and experiment characterizations in our previous studies.[1,6,8−10,19] Combining a simple geometric consideration with the electrochemical results in our previous studies; these structure features imply that the Pt_S/Ru_C NPs would gain the highest specific surface reaction sites among the experiment NPs.[9,20,21]

The crystal structures of Pt, PtRu alloy, and Pt_S/Ru_C NPs are further determined by XRD. Figure 3a−d compares the XRD patterns of Pt NPs, PtRu alloy, Pt_S/Ru_C, and Ru NPs annealed at 330 °C for 30 min. Clearly, the three NPs possess the fcc Pt crystallites (denoted by peaks C and D) but in different geometric configurations. (See Table 2.) For the case of PtRu alloy NPs, the upshift of diffraction peaks is mainly caused by the heteroatomic intermix of Ru atoms in Pt crystallite.[15] According to Bragg's law ($2d \sin \theta = n\lambda$, where λ is the incident X-ray wavelength), the lattice constant of the fcc Pt domain ($a_{(hkl)}$

associating with the interplanar spacing of the three facets ($d_{(hkl)}$) can be represented by eq 2

$$a = \frac{d_{(hkl)}}{\sqrt{h^2 + k^2 + l^2}} \tag{2}$$

where (hkl) denotes the miller index of reflection peak. The fitting curves and the structure parameters are given in Table 2. Accordingly, the lattice constant of Pt NPs ($a_{(111)}$ and $a_{(200)}$) is determined to be 3.91 ± 0.01 Å. For PtRu alloy NPs, the two diffraction peaks were found to be shifted by 0.1° to the high-angle region. The peak shift indicates the presence of lattice strain in Pt domains of NPs. The lattice strain of Pt crystal, s(Pt), in the bimetallic NPs is determined by the extent of their characteristic peaks offset from the peak of Pt NPs. With the careful background subtraction, the unexpected scattering

2257

dx.doi.org/10.1021/jp408012d | J. Phys. Chem. C 2014, 118, 2253−2262

interferences on the peak offset from the polymer retentions could be ruled out from the spectra. Herein, the lattice strain in the shell region could be estimated by eq 3

$$s(\text{Pt}) = \frac{a_{\text{Pt}} - a_{\text{ref}}}{a_{\text{ref}}} \times 100 \tag{3}$$

where a_{Pt} is the obtained Pt lattice parameter (i.e., Pt domain in our study). For PtRu alloy NPs, the diffraction peak at (111) facet is found slightly upshifted by 0.11°. The shortened lattice space could be attributed to the formation of Pt-to-Ru atomic intermixes which indicates the presence of a −0.32% expansive ε in the Pt region (crystal). Because the interatomic relocation is unavoidable, the peak upshift should be noticed in the XRD pattern of Pt_S/Ru_C bimetallic NPs. However, the downshift of diffraction peaks (extended lattice space) was noticed in the Pt_S/Ru_C NPs, where the characteristic peaks of metallic Pt facets (C and D) are shifted to the high-angle side from that of Pt NPs at a lattice space of 2.28 Å. It corresponds to a lattice constant of 3.95 Å and thus a 0.82% of lattice compression (ε) from that of Pt standard (with a lattice parameter of $a_{\text{ref}} = 3.92$ Å) due to the strong conjunction at the heterogeneous interface of RuO_2 core crystallites (i.e., formation of Pt_s/Ru_c).[21]

The average coherent length (ζ) of Pt NPs is determined to be 64.2 Å according to the Debye−Scherrer Equation (eq 4).

$$\zeta_{(hkl)} \approx \frac{0.9\lambda}{\beta_{(hkl)} \times \cos\theta} \tag{4}$$

where $\beta_{(hkl)}$ refers to the integral breadth of the diffraction peak and θ is the Braggs angle of the diffraction peaks, respectively.

The PtRu alloy NPs are a two-phase system. As shown in Figure 3b, the diffraction peaks A and B correspond to the characteristic signals from the (110) and (101) facets of the orthorhombic phase RuO_2 with a ζ of 84.9 and 91.7 Å, respectively. Because the peak width of Pt and RuO_2 diffractions lines are larger than 0.9 and 0.3°, it is inaccessible to extract the crystal structure parameters (i.e., the ζ of RuO_2 (200) facet and Pt (111) facet) by deconvoluting peak C. To avoid the overlap issues, we determined the crystal structure parameters from the peak D, where only the Pt (200) could be observed. By adopting the peak feature, the position, and peak width, the ζ is determined to be 32.3 Å. Two types of crystalline phase can be found in the Pt_S/Ru_C NPs. From Figure 3c, the metallic Pt (111) and (200) characteristics peaks are denoted by peaks C and D, respectively. The peaks A−C coincide with the diffractions of RuO_2 phase at (110), (101), and (200) facets. Again, according to the Scherrer equation, ζ for peaks A−C is determined to be 33.5, 30.5, and 26.6 Å, respectively. Because peak C comprises the diffraction lines of Pt (111) and RuO_2 (200) facets, it is understandable to notice the slight differences from the ζ of RuO_2 (200) to that of other RuO_2 facets and from the ζ of Pt (200) to that of Pt (111) because of peak overlapping. For the Pt shell crystal, the ζ for facets (111) and (200) is equal to 18.7 Å. Meanwhile, a considerable amount of interparticle intermix is observed (see Table S1 in the Supporting Information, XAS fitting) between Pt and Ru domains, so the lattice modulation of core−shell interface and restructure of Pt atoms in the shell to the Ru core are unavoidable and could be the possible reasons for the enlarged Pt ζ in comparison with the results of our SAXS.[9,10]

In summary, the coherent length (ζ) of Pt NPs, PtRu alloy NPs, and Pt_S/Ru_C NPs is determined to be 64.2, 32.3, and 18.7 Å, respectively. Such results are consistent with that obtained by the SAXS. For the cases of monometallic Pt and PtRu alloy NPs, the

ζ is normally smaller than the particle size determined by the SAXS. This is due to the smaller scattering cross section of crystallite phase than that of the particle surface (because there is always a thin layer of locally amorphous region at the particle surface with high density of defects). For the case of Pt_S/Ru_C NPs, the scattering cross section of Pt crystallite phase would merge to that of the Ru core region by a certain extent due to the interface lattice relaxation (which is believed to extend to about three atomic layers ∼10 Å) and the heteroatomic intermix (as indicated by Pt L_3-edge EXASF simulation shown in Figure S1 and Table S1 in the Supporting Information).[11] Hereby, the ζ would be larger than that of SAXS-determined shell thicknesses. The above structure information would be of vital importance because the lattice strain and the ζ would strongly correlate to the surface VB structure and the interface d-orbital charge relocation manners on the bimetallic NPs. The detailed structure evidence is provided by the results of SAXS and XAS later.

Intraparticle Structure Parameters of NPs. After the interparticle structure (i.e., sintering between NPs) is determined, the architectures of experiment NPs were determined by the small-angle X-ray scattering analysis, where the experiment spectra [$I(q)$ vs q] of Pt NPs, Pt_S/Ru_C NPs, and PtRu alloy NPs are shown in Figure 4a−c, respectively. The particle size distributions of these NPs were obtained by the Schultz distribution models, and the corresponding curves were presented in Figure 4d−f respectively. Here we discuss only the intraparticle structure information (i.e., particle shape, average size, and configuration, which are mostly shown by the scattering oscillation in the range $q > 0.08$ Å^{-1}) because the surface catalytic activity is the major concern. The structure parameters for the three types of NPs are obtained by fitting their SAXS spectra with adequate models. The obtained scattering functions were analyzed using a component SAXS model comprising fractal aggregates[17,22] and core−shell NPs models.[23] By considering a suspension of spherically symmetric core−shell particles with polydispersion, the scattering intensity can be expressed as the combination of the contributions from the fractal aggregate and the core−shell particle, as shown in eq 5

$$I(q) = A^{\text{F}} \cdot S(q)^{\text{F}} \cdot P(q)^{\text{F}} + A^{\text{CS}} \cdot S(q)^{\text{CS}} \cdot P(q)^{\text{CS}} \tag{5}$$

where A is the number density of the aggregates/particles. Both the structure factor $S(q)$ and the particle form factor $P(q)$ depend on the momentum transfer q. Symbols of F (fractal aggregate) and CS (core−shell particle) on the superscript indicate the corresponding models. $P(q)^{\text{F}}$ is the scattering from randomly distributed spherical "building block" particles, with radius R_0, volume fraction φ, and scattering length density difference $\Delta\rho = \rho_1 - \rho_2$, whereas the individual correlations of Pt NPs were fitted using a hard-sphere particle model. (The detailed interpretation of fitting functions is shown in ESI.) The obtained structure parameters are shown in Table 3. Accordingly, the Pt NPs and PtRu alloy NPs are grown in single spherical particle and possess an average particle size (D_{NPs}) of 43.8 and 30.4 Å with the polydispersity of particle size $P = 0.21$ and 0.13, respectively. The Pt_S/Ru_C NPs are grown into the core−shell particles. Core diameter (D_C) and shell thickness (T_S) are determined to be 31.8 and 4.2 Å (which refers to a number of shell atomic layers "Shell ALs" of 1.5 monolayers, as estimated by a simple numerical method in SI), respectively. The growth of NPs with a core−shell structure and precisely controlled shell thickness is evident because P of the particle size is quite small (∼0.08), as determined from the SAXS analysis.[21,24]

Table 3. Structure Parameters of Freshly Prepared Pt$_S$/Ru$_C$ NPs Determined by the SAXS[a]

NPs	D_C (Å)	T_S (Å)	D_{NPs} (Å)	shell ALs	P
Pt$_S$/Ru$_C$	31.8	4.2	40.2	1.5	0.08
Pt NPs			43.8		0.21
PtRu alloy			30.4		0.13

[a]Fitting parameters include the outer diameter D_{NPs}, the diameter of core D_C, the thicknesses of shell T_S, and the polydispersity parameter P. There are two additional parameters, namely, a scaling factor A and a q-independent background.

Valence Electron Structure of NPs. The above structural characterizations indicate the uniform size distribution of bimetallic PtRu NPs (i.e., in the form of alloy and core−shell structure). For the case of Pt$_S$/Ru$_C$ NPs, the shell crystal thickness can be precisely controlled in 1.5 atomic layers, resulting in a strongest compressive lattice strain (0.82%) among the experimental NPs. Such lattice compression dominates the VB structure and thus directly manipulates the surface reactivity of NPs. From previous DFT simulations and our studies,[1,6,9,11] the compressive strain is the major driving force for the heteroatomic interaction between Pt and Ru domains in bimetallic NPs. It not only enables the valence electron donation from Pt to Ru atoms but also prevents the Pt shell from chemisorption-induced lattice relaxation.[8,9] The strain effect on the charge donation is elucidated by the unfilled d states of NPs, which is quantified by a L-edges correlation developed by Mansour et al.[25,26] Figure 5 shows the Pt L_3-edge XANES spectra
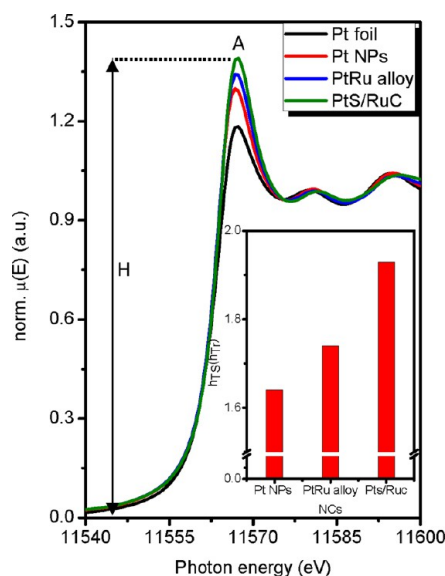
Figure 5. Pt L_3-edge XANES spectra of Pt foil, Pt NPs, PtRu alloy, and Pt$_S$/Ru$_C$ NPs. Inset shows the estimated unfilled Pt d-state of the three NPs.

of Pt NPs, PtRu alloy, Pt$_S$/Ru$_C$ NPs, and Pt foil. The absorption features at 11 564 eV correspond to the electronic transitions of 2p$_{3/2}$ to 5d$_{3/2}$ of Pt atoms, where the intensity (H) of the absorption hump at peak A (white line) reflects the orbital occupancy of the 5d orbital.[25] Herein, it is expected to note that the H value would increase with decreasing the 5d orbital occupancy of Pt atoms. Obviously, the strongest H value indicates the highest extent of charge donation from Pt to neighboring atoms (i.e., oxygen in platinum oxide and ruthenium

in Ru core) of Pt$_S$/Ru$_C$ among the three NPs. In the L-edges correlation analysis, the fractional change in the total number of unfilled d states (f_d) of the NPs compared with the number of the reference foil can be formulated as eq 6:

$$f_d = \frac{\Delta A_3 \sigma_3 + 1.11\Delta A_2 \sigma_2}{A_{3r}\sigma_3 + 1.11 A_{2r}\sigma_2} \tag{6}$$

After subtracting the Pt foil data from the NPs data, the resulting curves were then numerically integrated between −10 and 14 eV for both the L_2 and L_3 edges. In the data analysis, the absorption cross sections at the Pt L_3 (σ_3) and L_2 edge (σ_2) were set to be 117.1 and 54.2 cm^{-2} g^{-1}, respectively.[27] The variables A_{3r} and A_{2r} denote the integrated area of a standard Pt foil at L_3 and L_2 edges, respectively. In addition, the number of unfilled d states in the sample (h_{T_s}) can be represented by eq 7 if the number of unfilled d states in the reference material (h_{T_r}) is known:

$$h_{T_s} = (1 + f_d)h_{T_r} \tag{7}$$

The calculated h_{T_s} of Pt in the prepared NPs is shown in the inset of Figure 5. Accordingly, the h_{T_s} of Pt NPs is determined to be 1.64. Because the heteroatomic intermix is absent, the higher h_{T_s} of Pt NPs than Pt foil can be attributed to the particle size effect and to a certain extent of the surface oxidation.[4] For PtRu alloy NPs, the smaller (111) and (200) coherent length ($\zeta = 28.6−32.3$ Å, see Table 2) could be the main reason for the increased h_{T_s} due to a smaller coordination number (see Table S1 in the Supporting Information) and a similar extent of oxidation to that of Pt NPs (revealed by XPS in Table S2 in the Supporting Information). Pt$_S$/Ru$_C$ NPs show the highest h_{T_s} (~1.94), which suggests the highest extent of valence charge donation from Pt to neighboring coordinates. This is possibly due to its smallest ζ (~18.7 Å, see Table 2), the largest extent of surface oxidation (50.9%, see XPS analysis in Table S2 in the Supporting Information), and the heteroatomic Pt to Ru intermix "χ_{Pt}" (23.9%, see XAS analysis in Table S1 in the Supporting Information) among the three NPs.[1,6,9]

The proposed valence charge transition induced by the near-surface lattice strain and the heteroatomic intermix was further investigated by the VB photoemission spectroscopy. Figure 6 compares the VB spectra of Pt, PtRu alloy, and Pt$_S$/Ru$_C$ NPs. Accordingly, the VB of the Pt NPs consists of several features: a steep increase in the binding energy range of 0.00 to 0.24 eV, the flat stage with a reflection point at 0.72 eV (i.e., the surface E_b), a
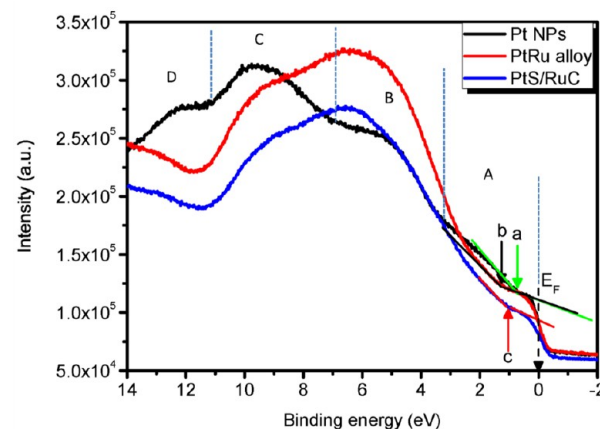
Figure 6. Valence band photoemission spectra of the three NPs investigated in this work.

shoulder until 3.38 eV (region A), and three additional broad bands centered at 5.27 (region B), 9.42 (region C), and 12.29 eV (region D). These distinguished features correspond to that of bulk Pt samples with ordered crystal facets, which resemble the metallic Pt 5d states. Compared with Pt NPs, the PtRu alloy NPs shift up the surface E_b by 0.56 eV (at 1.28 eV), merge the VB in A and B regions, and broaden and downshift the sublevel bands (C and D) by 3.01 eV. Because the intensity of the VB spectrum below the Fermi level is normalized to be same, the slight decrease in outer band (A region) intensity indicates a certain decrease in density of states (DOS) as that consistently revealed by the higher PtRu alloy h_{Ts} than Pt NPs in the inset of Figure 4. The Pt_S/Ru_C NPs possesses a higher surface E_b (at 1.16 eV) than Pt NPs and have a similar VB feature to PtRu alloy. In comparing with Ru NPs, the spectrum obtained here could not be regarded as the sum of separate ruthenium and platinum contributions because a substantial attenuation and modification on the VB features are found. Instead, it resembles the hybridization effects of sublayer crystal (in our study, the Ru core NPs) on outer layer atoms VB structures. Hereby, the substantial decreasing of the outer band (region A) intensity indicates a considerable decrease in DOS. It depicts the easy charge donation from Pt to the sublayer Ru atoms and the chemisorbed OH ligands[6] and therefore rationalizes the increase in E_b. Meanwhile, the downshift of sublevel bands and the substantial decrease in DOS imply the trend of valence charge injection at the topmost layer Pt atoms. These VB properties are consistent with the DFT predictions in the literature, suggesting the easy chemisorption and charge translocation from the anions to the Pt_S/Ru_C NPs surface sites. With such properties, the Pt_S/Ru_C NPs could reduce the onset potential for methanol electrooxidation to improve the DMFC performances.[1,9,10]

Electrochemical Performance of DMFC Module Equipped with the NPs@CNT Anode. The results of the structural characterizations show that the lattice strain, which is the dominating factor in the surface activity, is highly dependent on near-surface heteroatomic arrangements. From this information, it is conceivable to optimize the surface activity and Pt utilization of NPs by arranging their active atoms at different heterogeneous interfaces. This idea can be demonstrated by combining the structural parameters of heteroatomic intermix (see XAS analysis results in ESI), the nanoscaled architecture (see SAXS analysis in Figure 4 and Table 3), and the ECSA results. In addition, the obtained structural correlations provide direct implication for the electrochemical performance of the anodes coated with the NPs.

Figure 7a compares the CV curves of the three NPs in 0.5 M H_2SO_4. In general, both CV curves show the typical voltammetric behavior of Pt in acidic media,[28,29] and three regions could be qualitatively distinguished on these CV curves. In this Figure, the solid lines in black, red, and blue denote the CV curves of the Pt NPs, PtRu alloy, and Pt_S/Ru_C NPs, respectively. At potentials negative to ca. 0.36 V (region A), the reversible adsorption and desorption responses of hydrogen atoms (also called under-potential deposition hydrogen (UPD H)) are clearly found on the negative and positive sweeps, respectively. The voltammetric charge of the UPD H desorption is usually employed to estimate the ECSA (see later). The double-layer response region on the positive sweep of the black curve in Figure 6 (i.e., Pt NPs) is relatively narrow; meanwhile, cathodic currents are visible in this potential region, indicating that certain oxygen reduction occurs on both positive and negative sweeps at potentials negative to ca. 0.6 V. This statement is supported by the shift in the cathodic current density of ca. 0.5
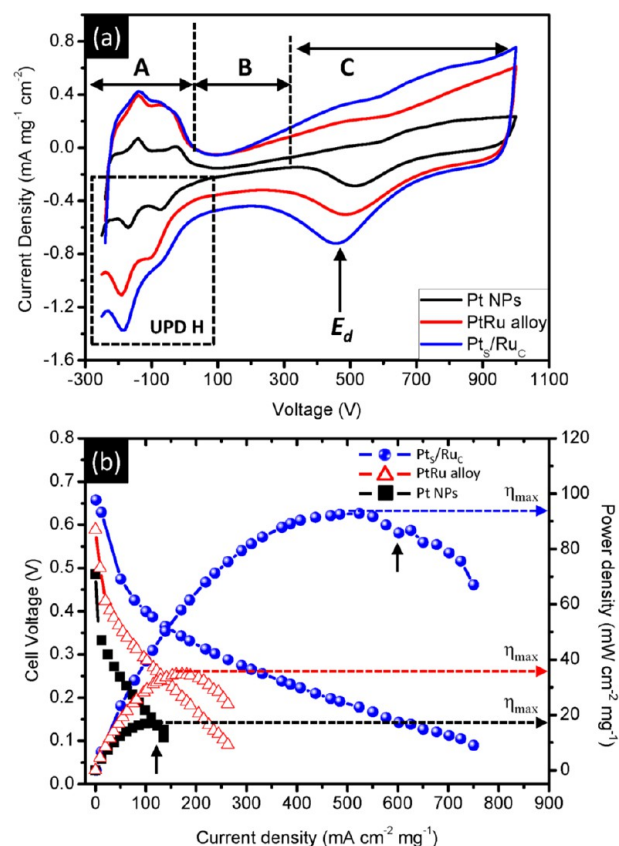

Figure 7. (a) Voltammetric behavior of the three NPs. All CV curves were measured at 30 mV s^{-1} in 0.5 M H_2SO_4. (b) Polarization curves of DMFC module assembled by CNT supported Pt NPs, PtRu alloy, and Pt_S/Ru_C NPs.

mA mg^{-1} on both positive and negative sweeps in this potential region. On the curves of PtRu alloy and Pt_S/Ru_C NPs, the background current density in the double-layer region is not constant, which gradually increases with the positive shift in the electrode potential. This phenomenon has been attributed to the presence of Pt adatoms on the shell surface, which are more easily oxidized.[28,29] Note the presence of a prepeak before the formation of Pt hydroxide or hydrated oxide ($Pt(OH)_2/PtO\cdot H_2O$) on the positive sweep of curves in Figure 7a, while there is no corresponding cathodic peak on the negative sweep. This prepeak in region C may be attributed to the oxidation of many Pt adatoms on the crystal edges of Pt shells and the surface of PtRu alloy NPs.[28,29]

From a comparison of solid curves in Figure 7a, the formation of monolayer Pt hydroxide prior to O_2 evolution occurs in the more positive potential region, which results in a positive shift in peak potential of oxide reduction on the black curve. The negative shift in the peak potential (E_d) of oxide reduction on Pt_S/Ru_C NPs in comparison with that on Pt NPs and PtRu alloy NPs could be associated with the particle size and Pt loading, as proposed in the literature,[30−32] as well as the strength of oxygen chemisorption at Pt sites,[33] while the former two factors could be ruled out in this case because Pt_S/Ru_C NPs show the largest particle size and the highest UPD hydrogen adsorption current densities (based on the same surface Pt loading) among the three NPs. Accordingly, the strength of oxygen chemisorption at Pt sites is believed to be responsible for the negative shift in the oxide reduction potential on Pt_S/Ru_C. This viewpoint is supported by the results reported by Mukerjee et al. from in

2260

dx.doi.org/10.1021/jp408012d | *J. Phys. Chem. C* 2014, 118, 2253−2262

situ XAS study and our HRTEM analysis (Figure 2) together. Therefore, the lower E_d on the curves in Figure 6a suggests the stronger bonding of oxygen onto interfacet regions of Pt_S/Ru_C (twin boundaries) NPs compared with the extended surfaces of Pt NPs and PtRu alloy NPs (flat surface).

The electrochemical surface area (ECSA) and surface atomic configurations of Pt are direct indexes for the performance of NPs. The ECSA of all NPs can be determined by integrating the voltammetric current densities in the UPD H desorption region of CVs (region E) according to eq 8:

$$\text{Pt ECSA } [\text{m}^2\ \text{g}^{-1}] = \frac{(Q_{\text{H-des}}[C]) \times 100}{210\ \mu\text{C cm}^{-2} \cdot (w_{\text{Pt}}[\text{g}])} \tag{8}$$

where $Q_{\text{H-des}}$ refers to the voltammetric charge density resulting from H desorption; meanwhile 210 μC cm^{-2} is the standard hydrogen desorption charge (a factor) corresponding to unit surface area of Pt. Interestingly, the ECSA of Pt NPs is only equal to 74.7 m^2 g^{-1}, which is much smaller than that of the Pt_S/Ru_C NPs (159.6 m^2 g^{-1}). From geometric standpoints, the interparticle sintering effect on the ECSA is negligible because the particle volume of the three NPs on the electrode differs by only 3−5% (as revealed by XRD in Table S3 in the Supporting Information) with respect to that of a freshly prepared sample. This phenomenon implies that the activities of NPs are mainly controlled by their surface atomic configurations. For Pt_S/Ru_C, the core−shell-type NPs contain a high ratio of interfacet boundaries. Consistent with the features of the oxide reduction, these boundaries contain a high density of defects (including corners, edges, steps, and terraces) with high-coordination sites for the UPD H adsorption/desorption, leading to the improved ECSA.

Our CV analysis indicates that the type of heterogeneous conjunction around the active atoms (i.e., Pt) is the dominating factor in the activity of NPs.[8,34] From the previous structural characterizations, one can notice that the heterogeneous conjunctions on Pt_S/Ru, PtRu alloy, and Pt NPs can be classified as (1) Pt atoms on top of heterogeneous Ru lattice (Pt@Ru); (2) Pt atoms conjunct to individual Ru atoms (Pt−Ru); and (3) Pt atoms on top of Pt lattice (Pt−Pt), respectively. Among the three types, the Pt@Ru gains the highest compressive lattice strain in the Pt region. The lattice strain generates a strong heteroatomic hybridization between Pt and Ru atoms at the interface region. It triggers a valence charge donation from Pt to Ru atoms, splitting the Pt VBs, and thus substantially improves the activity (including the site regenerating and reactivity kinetics) of active atoms. For the case of PtRu alloy, only individual heteroatomic conjunction is induced, which gives raise to the bifunctional mechanism and the ligand effect on the particle surface. These two pathways improve the performance of Pt atoms by a certain extent but are sufficiently lower than that offered by the lattice strain effect.[1,6,35]

The surface reactivity of NPs directly influences the performance of DMFC. The polarization curves of DMFCs with the three NPs in the methanol solution (1 M, 60 mL h^{-1}) and air operation mode are shown in Figure 7b. (The polarization curves for each DMFC on an adequate scale are given in Figure S2 in the Supporting Information.) Accordingly, the DMFC with Pt NPs exhibits an open-circuit voltage (OCV) of 0.49 V and delivers a maximum power density (η_{max}) of 17.1 (mW cm^{-2} mg^{-1}). Two segments (denoted by arrow in dashed line) are found in the polarization curve, which suggests the large interfacial contact resistance among Pt NPs, CNT/CF support, and methanol

chemisorptions. This is attributable to the fact that Pt NPs tend to aggregate and sinter into bulk at a heterogeneous surface because of the strong preference of Pt restructure in reducing the total surface energy of Pt[12,36] and the strong CO-poison bonding at the Pt NPs.[5] In comparing with Pt NPs, the PtRu alloy improves the OCV and η_{max} of DMFC by ca. 0.1 V (from 0.49 to 0.59 V) and ∼100% (from 17.1 to 35.1 mW cm^{-2} mg^{-1}), respectively. Such improvements are consistent with that in the literature and could mainly be attributed to the influences of the bifunctional mechanisms and ligand effects.[37] Only a single segment is found in the polarization curve, which indicates the improved interface contact between NPs and CNT/CF support due to the strong preference of Ru to carbon bonding[38] and the impeded interparticle sintering. (See HRTEM in Figure 2.) By adopting Pt_S/Ru_C NPs to the anode, the OCV and η_{max} of DMFC are improved by 0.18 V (from 0.49 to 0.67 V) and ∼450% (from 17.1 to 92.8 mW cm^{-2} mg^{-1}), respectively, in comparison with that using Pt NPs. Considering the influences of PtRu alloy NPs on OCV and η_{max}, the substantial enhancements by Pt_S/Ru_C NPs seem surprising. However, this phenomenon can be rationalized by its Pt valence electronic properties. In Pt_S/Ru_C NPs, the Pt atoms possess a substantial lower VB level and DOS compared with those in Pt NPs and PtRu alloy NPs. This is caused by the valence charge donation from Pt to the neighboring atoms due to the compressive strain in the shell crystal region. Consequently, the Pt_S/Ru_C NPs provide the hydrophilic environments[6] that facilitate chemisorption and weaken the carbonaceous bonding at its surface.[1,8,9] Such physiochemical properties are confirmed by its less positive onset potential (strong driving force) for methanol oxidation and the outstanding selective oxidation of carbon monoxide at room temperature in comparison with the NPs in other configurations (i.e., bulk, alloy, or thin films).[1,6] Similar to the case of Pt NPs, the polarization curve of Pt_S/Ru_C shows two segments (denoted by the arrow in blue). Although these features suggest the existence of considerable extent of contact resistances at interfaces between the Pt_S/Ru_C NPs and CNT/CF support, the Pt_S/Ru_C NPs still possess better performances than Pt NPs and PtRu alloy NPs. Here all DMFCs with the NPs@CNT anode show relatively worse performances in comparison with that demonstrated in other literature. This is probably due to the fact that our NP-based CNT anodes have not been optimized for the DMFCs compared with the state-of-the-art DMFC systems.

■ CONCLUSIONS

In this study, we developed a novel synthetic technique capable of growing the core−shell type nanocatalysts with precise control of the shell thickness to 1.5 atomic layers. This type of catalyst possesses several unique electrochemical properties promising to the DMFC application. Compared with the DMFC with the Pt NPs anode, the core−shell NPs save 60% or higher Pt usage, increase the OCV by 0.18 V (at 0.67 V), and enhance the η_{max} by ∼450% (at 92.8 mW cm^{-2} mg^{-1}). These promotions are more than double that of DMFC with conventionally PtRu alloy NPs and Pt NPs. Our systematic and mechanistic interpretations clearly demonstrate that such dramatic enhancements originate from the lattice compression in the Pt shell crystal. The strain triggers a substantial valence charge donation from Pt to Ru, increases the E_b by 0.44 eV, and lowers the VB level by 0.31 eV. By such VB modification, it improves the surface activity for chemisorption and electrooxidation of methanol, accelerates the carbon monoxide oxidation, and promotes the anodic reaction kinetic of the DMFC system. More importantly, this convincing

evidence indicates that the Pt_S/Ru_C NPs are promising to the development of high-performance, cost-effective, and eco-friendly DMFCs.

■ ASSOCIATED CONTENT

ⓢ Supporting Information

XRD data collection and analysis, the XPS results, and the XAS results. The procedures for assembling the DMFC stack, the corresponding characterization curves, and experiment conditions are enclosed. This material is available free of charge via the Internet at http://pubs.acs.org.

■ AUTHOR INFORMATION

Corresponding Authors
*Tsan-Yao Chen: E-mail: chencaeser@gmail.com.
*Tsang-Lang Lin: Tel: +886-3-5742671. Fax: +886-3-5728445. E-mail: tllin@mx.nthu.edu.

Author Contributions
[#]J.-J.W. and Y.-T.L. have equally contributed to this study.

Notes
The authors declare no competing financial interest.

■ ACKNOWLEDGMENTS

■ REFERENCES

(1) Adzic, R. R.; Zhang, J.; Sasaki, K.; Vukmirovic, M. B.; Shao, M.; Wang, J. X.; Nilekar, A. U.; Mavrikakis, M.; Valerio, J. A.; Uribe, F. *Top. Catal.* **2007**, *46*, 249−262.

(2) Besenbacher, F.; Chorkendorff, I.; Clausen, B. S.; Hammer, B.; Molenbroek, A. M.; Nørskov, J. K.; Stensgaard, I. *Science* **1998**, *279*, 1913−1915.

(3) Hwang, B. J.; Sarma, L. S.; Chen, J. M.; Chen, C. H.; Shih, S. C.; Wang, G. R.; Liu, D. G.; Lee, J. F.; Tang, M. T. *J. Am. Chem. Soc.* **2005**, *127* (31), 11140−11145.

(4) Hwang, B.-J.; Kumar, S. M. S.; Chen, C.-H.; Chang, R.-W.; Liu, D.-G.; Lee, J.-F. *J. Phys. Chem. C* **2008**, *112*, 2370−2377.

(5) Hogarth, M. P.; Ralph, T. R. *Platinum Met. Rev.* **2002**, *46* (4), 117−135.

(6) Alayoglu, S.; Nilekar, A. U.; Mavrikakis, M.; Eichhorn, B. *Nat. Mater.* **2008**, *7*, 333−338.

(7) Alayoglu, S.; Eichhorn, B. *J. Am. Chem. Soc.* **2008**, *130*, 17479−17486.

(8) Sasaki, K.; Naohara, H.; Cai, Y.; Chio, Y. M.; Liu, P.; Vukmirovic, M. B.; Wang, J. X.; Adzic, R. R. *Angew. Chem., Int. Ed.* **2010**, *49*, 8602−8607.

(9) Chen, T.-Y.; Luo, T.-J. M.; Yang, Y.-W.; Wei, Y.-C.; Wang, K.-W.; Lin, T.-L.; Wen, T.-C.; Lee, C.-H. *J. Phys. Chem. C* **2012**, *116*, 16969−16978.

(10) Chen, T.-Y.; Lin, T.-L.; Luo, T.-J. M.; Chio, Y.; Lee, J.-F. *ChemPhysChem* **2010**, *11* (11), 2383−2392.

(11) Schlapka, A.; Lischka, M.; Gross, A.; Kasberger, U.; Jakob, P. *Phys. Rev. Lett.* **2003**, *91*, 016101.

(12) Bligaard, T.; Nørskov, J. K. *Electrochim. Acta* **2007**, *52*, 5512−5516.

(13) Tsao, C.-S.; Tzeng, Y.-R.; Yu, M.-S.; Wang, C.-Y.; Tseng, H.-H.; Chung, T.-Y.; Wu, H.-C.; Yamamoto, T.; Kaneko, K.; Chen, S.-H. *J. Phys. Chem. Lett.* **2010**, *1*, 1060−1063.

(14) Watanabe, M.; Motoo, S. *J. Electroanal. Chem.* **1975**, *60*, 275−283.

(15) Chen, T.-Y.; Liu, Y.-T.; Chen, H.-S.; Wang, K.-W.; Yang, C.-T.; Luo, T.-J. M.; Lee, C.-H.; Lin, T.-L. *CrystEngComm* **2013**, *15*, 3932−3942.

(16) Chen, T.-Y.; Lin, T.-L.; Chen, C.-C.; Chen, C.-M.; Chen, C.-F. *J. Chin. Chem. Soc.* **2009**, *56*, 1236−1243.

(17) Lin, J.-M.; Lin, T.-L.; Jeng, U.-S.; Zhong, Y.-J.; Yeh, C.-T.; Chen, T.-Y. *J. Appl. Crystallogr.* **2007**, *40*, s540−s543.

(18) Sun, Y.; Xia, Y. *Adv. Mater.* **2002**, *14*, 833−837.

(19) Lo, S. H. Y.; Chen, T.-Y.; Wang, Y.-Y.; Wan, C.-C.; Lee, J.-F.; T.-L., L. *J. Phys. Chem. C* **2007**, *111*, 12873−12876.

(20) Chen, T.-Y.; Chen, I.-L.; Liu, Y.-T.; Lin, T.-L.; Yang, P.-W.; Wu, C.-Y.; Hu, C.-C.; Luo, T.-J. M.; Lee, C.-H. *CrystEngComm* **2013**, *15*, 982−994.

(21) Chen, T.-Y.; Liu, Y.-T.; Nguyen, H. M.; Fan, L.-J.; Wu, C.-Y.; Luo, T.-J. M.; Lee, C.-H.; Yang, Y.-W.; Wen, T.-C.; Lin, T.-L. *J. Mater. Chem. A* **2013**, *1*, 5660−5669.

(22) Teixeira, J. *J. Appl. Crystallogr.* **1988**, *21*, 781−785.

(23) Bartlett, P.; Ottewill, R. H. *J. Chem. Phys.* **1992**, *96*, 3306.

(24) Wagner, J. *J. Appl. Crystallogr.* **2004**, *37*, 750−756.

(25) Reifsnyder, S. N.; Otten, M. M.; Sayers, D. E.; Lamb, H. H. *J. Phys. Chem. B* **1997**, *101*, 4972−4977.

(26) Mansour, A. N.; Cook, J. W.; Sayers, D. E. *Chem. Phys.* **1984**, *88*, 2330.

(27) McMaster, W. H.; Grande, N. K. D.; Hubell, J. H.; Mallett, J. H. *Compilation of X-ray Cross Sections*; National Technical Information Service: Springfield, VA, 1969.

(28) Hu, C.-C.; Liu, K.-Y. *Electrochim. Acta* **1999**, *44*, 2727−2738.

(29) Hu, C.-C.; Liu, K.-Y. *Electrochim. Acta* **2000**, *45*, 3063−3068.

(30) Maillard, F.; Eikerling, M.; Cherstiouk, O. V.; Schreier, S.; Savinova, E.; Stimming, U. *Faraday Discuss.* **2004**, *125*, 357−407.

(31) Kabbabi, A.; Gloaguen, F.; Andolfatto, F.; Durand, R. *J. Electroanal. Chem.* **1994**, *373* (1−2), 251−254.

(32) Frelink, T.; Visscher, W.; van Veen, J. A. R. *J. Electroanal. Chem.* **1995**, *382* (1−2), 65−72.

(33) Mukerjee, S.; McBreen, J. *J. Electroanal. Chem.* **1998**, *448* (2), 163−171.

(34) Mayrhofer, K. J.; Juhart, V.; Hartl, K.; Hanzlik, M.; Arenz, M. *Angew. Chem., Int. Ed.* **2009**, *48* (19), 3529−3531.

(35) Strasser, P.; Koh, S.; Anniyev, T.; Greeley, J.; More, K.; Yu, C.; Liu, Z.; Kaya, S.; Nordlund, D.; Ogasawara, H.; Toney, M. F.; Nilsson, A. *Nat. Chem.* **2010**, *2*, 454−460.

(36) Ding, Y.; Sun, X.; Wang, Z. L.; Sun, S. *Appl. Phys. Lett.* **2012**, *100*, 111603.

(37) Roth, C.; Benker, N.; Buhrmester, T.; Mazurek, M.; Loster, M.; Fuess, H.; Koningsberger, D. C.; Ramaker, D. E. *J. Am. Chem. Soc.* **2005**, *127*, 14607−14615.

(38) Murray, J. P.; Steinfeld, A.; Fletcher, E. A. *Energy* **1995**, *20*, 695−704.